Dalton Transactions

ROYAL SOCIETY OF CHEMISTRY

PAPER

View Article Online
View Journal | View Issue

Cite this: *Dalton Trans.*, 2026, **55**, 4677

Acid–responsive rhenium(I) NHC complexes: pyrazine *vs.* pyridine

Pedro O. Abate,[a,b,c,d] José Francisco Rizo,[a,b] Francisco José Fernández-de-Córdova,[b] Abel Ros *[b] and Orestes Rivada-Wheelaghan *[a,b]

Received 21st January 2026,
Accepted 19th February 2026

DOI: 10.1039/d6dt00158k

rsc.li/dalton

Four rhenium(I) tricarbonyl complexes featuring pyridine- or pyrazine-functionalized N-heterocyclic carbenes were synthesized and fully characterized, including the determination of their molecular structures by single-crystal X-ray diffraction. Electrochemical and spectroelectrochemical measurements were performed. The development of isosteric Re(I) complexes enabled a direct comparison of how Brønsted and Lewis acids influence their electronic properties. Complexes containing the pyridyl core showed no detectable changes in either electrochemical or spectroscopic studies. In contrast, those bearing the pyrazine fragment exhibited significant shifts at both reductive and oxidative potentials, attributable to the extra nitrogen atom in the 1,4-diazine ring, which can interact with Brønsted (and Lewis) acids. In this regard, comparison of alkali salts with Brønsted acids revealed that the presence of the latter induces substantially larger electronic perturbations.

Introduction

Multifunctional ligands can bind to metal centers, interact with other molecules, or respond to stimuli through additional functionalities in their structures.[1] In homogeneous catalysis, metal–ligand cooperation may serve as an example in which both the metal and the multifunctional ligand act in concert,[2] either through redox stabilization,[3] or through direct interaction with chemical bonds enabling the desired reactivity.[4] However, as is often the case, the best example is observed in nature and involves enzyme activity modulation by the binding of a regulatory molecule to a site distinct from the active site.[5] The synergistic process of *allosteric regulation* has inspired synthetic chemists to build and modulate functional supramolecular structures,[6–8] to fine-tune the electronic properties of "simple" molecules,[9–11] or to develop switchable catalysis,[12,13] thereby expanding their applicability.[14] For example, owing to the selective capacity of polyether motifs to bind alkali cations in solution, their rational addition proximal to the metal-binding site in different ligands[15–22] has helped to develop systems that respond to stimuli. This has allowed the modification of the redox properties of many systems using non-redox-active additives,[18,20,23,24] either to promote redox transformations at potentials other than the original ones[25,26] or to facilitate the activation of molecules.[27,28]

Alternatively, others have developed their ligand scaffolds with the stimuli-responsive group located in regions remote from the reactive center.[29–32] Thus, the reactivity and electronic properties of the complex vary with the addition of a Lewis[33–36] or Brønsted acid,[30,37,38] without directly involving the first coordination sphere. Building on the concept of remotely modulating electronic properties, we have designed a pyrazine (pz)-based ligand to systematically investigate how Brønsted and Lewis acids influence the electronic characteristics of the metal complex. Building blocks based on 1,4-diazine have been used in the assembly of molecular aggregates,[39–41] and they are well known for their capacity to facilitate charge delocalization among multiple metal centers.[40,42–44] Moreover, there has been an increase in reports of coordination complexes bearing ligands with a pz core targeting new avenues of reactivity and catalysis, which have undoubtedly led to a greater understanding of these frameworks.[45–47] Pincer-type ligands represent the most common platform, with substituted groups such as: bis(imino)-pz,[48,49] bisphosphine-pz,[40,50,51] and N-heterocyclic carbenes (NHCs), among others.[52] Interestingly, across all the literature reviewed, we found no reports in which the effects of

[a]*Departamento de Química Inorgánica, Universidad de Sevilla, C/Prof. García González 1, 41012 Seville, Spain. E-mail: orivada@us.es*
[b]*Instituto de Investigaciones Químicas, Centro de Innovación en Química Avanzada (ORFEO-CINQA), Consejo Superior de Investigaciones Científicas – Universidad de Sevilla, C/Américo Vespucio 49, 41092 Seville, Spain. E-mail: abel.ros@iiq.csic.es*
[c]*Universidad de Buenos Aires, Facultad de Ciencias Exactas y Naturales, Departamento de Química Inorgánica, Analítica y Química Física, Pabellón 2, Ciudad Universitaria, C1428EHA Buenos Aires, Argentina*
[d]*CONICET – Universidad de Buenos Aires. Instituto de Química-Física de Materiales, Ambientes y Energía (INQUIMAE), Pabellón 2, Ciudad Universitaria, C1428EHA Buenos Aires, Argentina*

adding Brønsted and/or Lewis acids to pz-substituted complexes have been systematically examined. Therefore, we report the synthesis and characterization of rhenium(I) tricarbonyl complexes stabilized by pyridine (py)- and pz-functionalized NHC ligands, along with a systematic investigation of the effects of Brønsted and Lewis acid additives on their electronic properties.

Results and discussion

Syntheses and crystal structure

The two imidazolium precursors synthesized (**ClHL^{Py}**: 3-mesityl-1-(pyridin-2-ylmethyl)-1*H*-imidazol-3-ium; and **ClHL^{Pz}**: 3-mesityl-1-(pyrazin-2-ylmethyl)-1*H*-imidazol-3-ium) were prepared in two steps starting from 2-(chloromethyl)pyridine and 2-(chloromethyl)pyridine, respectively. The 2-(chloromethyl)pyrazine was obtained by a radical reaction with *N*-chlorosuccinimide.[53] The corresponding substrates were later reacted with 1-mesityl-1*H*-imidazole to obtain the desired **ClHL^{Py}** and **ClHL^{Pz}** precursors. For the synthesis of the neutral rhenium complexes, a well-established methodology was followed.[54] Thus, the corresponding azolium salt was treated with Ag_2O to generate the silver carbene intermediates after 24 h at room temperature under dark stirring, and these were then transmetallated to $[ReCl(CO)_5]$ to afford the neutral complexes **1**, $[Re(Cl)(CO)_3(L^{Py})]$, and **2**, $[Re(Cl)(CO)_3(L^{Pz})]$, in 77% and 66% yields, respectively (Scheme 1, top). Due to solubility issues, this reaction step required 48 h of heating (at 40 °C). To obtain the cationic acetonitrile adducts **3·X**, $[Re(CH_3CN)(CO)_3(L^{Py})][X]$, and **4·X**, $[Re(CH_3CN)(CO)_3(L^{Pz})][X]$, the complexes **1** and **2** were treated with the corresponding silver salt (AgX) in a solvent mixture containing acetonitrile (X = BF_4, PF_6 or OTf). To avoid anion effects during electrochemical measurements, the triflate anion was replaced with PF_6 by treatment with an aqueous NH_4PF_6 solution (see SI). Thus, following Method A or B (Scheme 1, bottom), cationic complexes **3·X** and **4·X** were obtained in moderate to good yields (34–87%).

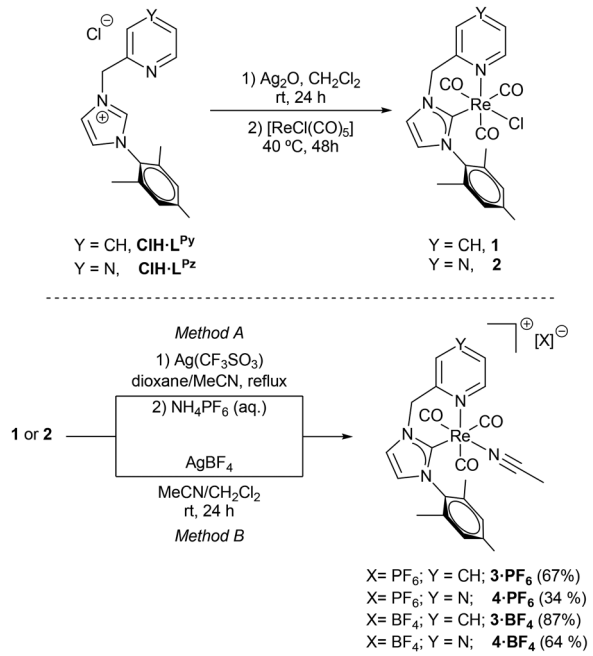

Scheme 1 Synthesis of neutral and cationic Re^{I} complexes **1–4**.

With respect to the spectroscopic properties of neutral complexes **1** and **2**, the ^{1}H-NMR spectra exhibit the common diastereotopic pattern of the methylene benzylic protons (doublets around 5.3–5.4 and 6.2–6.3 ppm) and the inequivalence of the methyl groups of the mesityl fragment, which indicates the bidentate bearing of the NHC–N ligand. This is also corroborated by ^{13}C NMR, which shows the $C_{carbene}$ resonance around 182–183 ppm and only three carbonyl groups in the 191–197 ppm region. In the case of cationic complexes **3·PF$_6$** and **4·PF$_6$**, the acetonitrile adduct is corroborated by ^{1}H and ^{13}C NMR spectra, showing signals at 2.37 and 3.7 ppm, respectively, attributed to the methyl group of the coordinated acetonitrile molecule. Due to the π-acceptor capability of the CH_3CN ligand compared to chloride, the π-retrodonation to the *NHC* and CO groups is less efficient in complexes **3·PF$_6$** and **4·PF$_6$**, and therefore the chemical shifts of the $C_{carbene}$ and CO groups are shielded by ∼3–4 ppm with respect to neutral complexes **1–2**. These structural features could also be confirmed by IR measurements (Fig. 1 and Table 1). The intense carbonyl bands observed in $Re(CO)_3$ complexes with α-diimine or carbene-type ligands are sensitive to the electron-accepting properties of the coordinated ligands. Table 1 summarizes the experimental and DFT-calculated carbonyl stretching frequencies of complexes **1–2** and **3–4·PF$_6$**. As shown in Table 1, all complexes display three bands assigned to the A′(1), A″, and A′(2) vibrational modes, consistent with a facial geometry of the carbonyls.[55,56] Replacement of the py ring with a stronger π-acceptor, such as pz, has only a minor effect on the stretching frequencies, causing an average blue shift of ≈5 cm^{-1}. When the chloride ligand is replaced by the π-acceptor

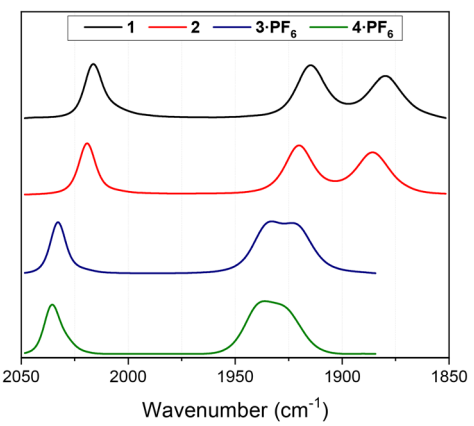

Fig. 1 IR spectra of complexes **1**, **2**, **3·PF$_6$** and **4·PF$_6$** in CH_3CN at room temperature.

Table 1 Experimental and calculated CO vibrational frequencies of complexes **1**, **2**, **3·PF$_6$** and **4·PF$_6$** in acetonitrile at room temperature

	ν/cm^{-1} (DFT)			
Compound	A′(1)	A″	A′(2)	k_{av}[a] (N m^{-1})
1	2017 (2027)	1915 (1921)	1880 (1895)	1517
2	2019 (2030)	1920 (1928)	1886 (1901)	1523
3·PF$_6$	2033 (2041)	1933 (1941)	1923 (1933)	1557
4·PF$_6$	2035 (2042)	1940[b] (1941)	1926[b] (1932)	1563

[a] Average carbonyl force constant (k_{av}) calculated as $k_{av} = 4.0383 \times 10^{-4} \frac{\sum_i g_i \nu_i}{\sum_i g_i}$, where g_i is the degeneracy of the ith carbonyl stretching mode of frequency ν_i (cm^{-1}). [b] Bands obtained from Lorentzian deconvolution (Fig. S25).

CH_3CN, all the carbonyl stretching frequencies exhibit a more pronounced blue shift, with an average of ≈40 cm^{-1}.

The magnitude of the shift in the carbonyl stretching frequencies of **1** *vs.* **3·PF$_6$** or **2** *vs.* **4·PF$_6$** can be correlated with changes in the bond orders, derived from the average carbonyl force constants calculation (k_{av}).[57] An increase in the k_{av} value is indicative of a decrease in π-backdonation from the rhenium center to the carbonyl ligands. As shown in Table 1, k_{av} increases when Cl$^-$ is replaced by CH_3CN, consistent with the enhancement of the CO bond order.

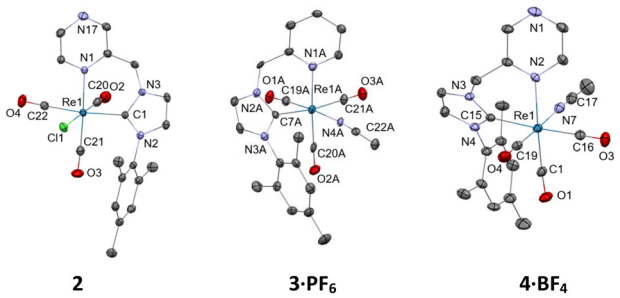

Fig. 2 X-ray structures of complexes **2**, **3·PF$_6$**, and **4·BF$_4$**. Structures are shown with 50% displacement ellipsoids. Non-coordinating anions and solvents are omitted for clarity. Selected bond lengths (Å): **2**: C1–Re1 = 2.488(1); C1–Re1 = 2.165(3); C22–Re = 1.952(4); N1–Re = 2.221(3). **3·PF$_6$**: C7A–Re1A = 2.174(8); C20A–Re1A = 1.91(1); C21A–Re1A = 1.957 (9); N1A–Re1A = 2.229(7). **4·BF$_4$**: C15–Re = 2.169(4); C1–Re = 1.922(4); C16–Re = 1.945(4); N2–Re = 2.213(3).

All these structural features observed in solution could be corroborated in the solid state by X-ray diffraction analysis. Thus, as shown in Fig. 2, the neutral complex **2** and the cationic complexes **3·PF$_6$** and **4·BF$_4$** adopt a distorted octahedral geometry with chirality at the Re center (although the crystallographic unit cell contains both enantiomers, only one is shown in the figure). The 3 carbonyl groups adopt a facial geometry, consistent with the results observed in the IR studies. No differences are observed in the structure when a different counter anion is present, as X-ray diffraction studies were obtained for complex **3·PF$_6$** and **3·BF$_4$** (see SI). Similarly, no significant changes are observed in the structure when the chloride ligand is exchanged for acetonitrile from **2** to **4·BF$_4$**. Regarding the bond distances, the Re–CO bond distances *trans* to the carbene moiety are slightly elongated (~1.95 Å) as compared to the others (~1.92 Å), due to the *trans* influence of the carbene ligand.

Electrochemistry

The electrochemical measurements were performed in dry CH_3CN solution with 0.1 M Bu_4NPF_6 as the supporting electrolyte, using a glassy carbon working electrode, a Pt counter electrode (CE), and a saturated calomel electrode (SCE) as the reference electrode (at constant temperature of 293 K) at a scan rate of 0.1 V s^{-1}. Table 2 shows the redox potentials of complexes **1**, **2**, **3·PF$_6$** and **4·PF$_6$**, obtained under these conditions. As expected for NHC-based rhenium complexes, these compounds exhibit metal-centered oxidations and ligand-centered reductions, respectively. For the neutral complexe the $Re^{2+/+}$ couples were detected at 1.18 V, 1.27 V, 1.66, and 1.73 V, for **1**, **2**, **3·PF$_6$** and **4·PF$_6$**, respectively. These values are consistent with those previously reported for analogous complexes.[54] The differences observed between complexes **1** *vs.* **2** and **3·PF$_6$** *vs.* **4·PF$_6$** are attributed to the substitution of the py ring with a pz ring in the carbene ligand. Since pz is a more π-accepting (electron-withdrawing) ligand,[45] it stabilizes the Re (dπ t_{2g}) orbitals, resulting in an anodic shift of ~90 mV of the $Re^{2+/+}$ couple (Fig. 3).

On the other hand, comparison between the complexes having the same carbene ligand and varying the axial ligand, from Cl$^-$ to CH_3CN, renders a shift of *ca.* 50 mV of the $Re^{2+/+}$ couples. As shown in their cyclic voltammograms (Fig. S26–S29, SI pages S24–S27), these processes are quasi-reversible in nature, with a slight increase in reversibility when the Cl$^-$ is

Table 2 Reduction potentials and absorption spectroscopic data of complexes **1**, **2**, **3·PF$_6$** and **4·PF$_6$** in acetonitrile at room temperature

	$E_{1/2}$ (ΔE_p)[a]/V[b] (mV)				
Compound	$Re^{2+/+}$	$L^{0/-1}$	ΔE_{ML}/V[c]	λ_{max}/nm (ν_{max}/cm^{-1})	ε/M^{-1} cm^{-1}
1	1.18 (80)	−1.99 (irr.)	3.17	308 (32468)	4213
2	27 (100)	−1.36 (irr.)	2.63	348 (28736)	2560
3	1.66 (80)	−1.73 (irr.)	3.39	296 (33784)	6706
4	1.73 (90)	−1.15 (irr.)	2.88	313 (31152)	8180

[a] $\Delta E_p = |E_a| - |E_c|$. [b] $E_{1/2}$ *vs.* SCE. [c] $\Delta E_{ML} = E_{1/2}^{Re^{2+/+}} - E_{1/2}^{L^{0/-1}}$.

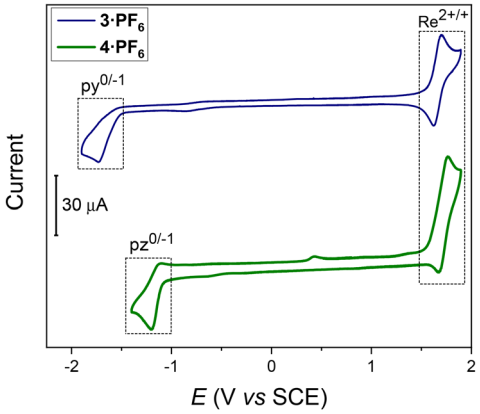

Fig. 3 Oxidative and reductive Cyclic Voltammetry of $3{\cdot}PF_6$ (blue) and $4{\cdot}PF_6$ (green) in CH_3CN 0.1 M Bu_4NPF_6 at 293 K. v = 100 mV s^{-1}. [complex] = 1 mM.

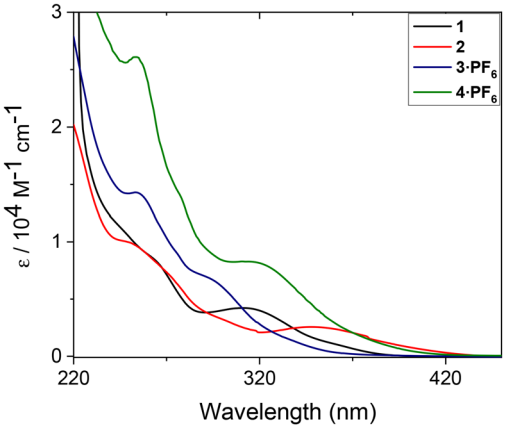

Fig. 4 UV-Vis spectra of complexes **1**, **2**, $3{\cdot}PF_6$ and $4{\cdot}PF_6$ in CH_3CN at room temperature.

replaced by CH_3CN. This behavior can be attributed to the formation of the solvento complex after one-electron oxidation of the neutral complexes.[58,59] Scan rate studies were conducted for the $Re^{2+/+}$ couples of the four complexes; in all cases, the processes were diffusion-controlled as evidenced by the linear dependence of the peak current on the square root of the scan rate (Fig. S26–S29, pages S24–S27).[60]

The ligand-centered reduction processes were detected at −1.99 V (**1**), −1.36 V (**2**), −1.73 V ($3{\cdot}PF_6$), and −1.15 V ($4{\cdot}PF_6$), respectively. All these redox couples are described as one-electron transfer processes. In complexes **1** and $3{\cdot}PF_6$, the reductions are assigned to the $py^{0/-1}$ couple, whereas in complexes **2** and $4{\cdot}PF_6$, they are $pz^{0/-1}$-based. The shift of around 600 mV in the $L^{0/-1}$ reduction potential of the complexes containing py *vs.* pz arises from the enhanced electron-withdrawing ability of pz *vs.* py, resulting in an anodic shift of the $pz^{0/-1}$ reduction potential.

DFT calculations of the one-electron oxidized and one-electron reduced species of complexes **1**, **2**, $3{\cdot}PF_6$, and $4{\cdot}PF_6$ were performed to gain a better understanding of the electronic structure. DFT calculations were performed using the PBE1PBE (PBE0) hybrid functional.[61] Re(I) was described with the LANL2DZ basis set with the corresponding ECP, all non-metal atoms were treated with the 6-311G(d,p) basis set.[62–64] Dispersion interactions are taken into account with the Grimme dispersion correction with Becke–Johnson damping.[65,66] All the calculations were done using the con all the calculations were done by using the conductor-like polarizable continuum model (CPCM).[67,68] Calculated Spin densities (SDs) support the assignment of the redox events (Table S2, SI page S29). On the other hand, the SDs of the oxidized complexes help to rationalize the greater influence of the axial substitution relative to the equatorial substitution in the reduction potential of the $Re^{2+/+}$ couple. As the one-electron oxidation involves the HOMO, which is a d_{xz} (Re) orbital, ligand substitution along the z-axis is expected to induce a stronger stabilization of this orbital than substitution in the equatorial plane (pz *vs.* py). Consequently, this stronger stabilization shifts the $Re^{2+/+}$ couple cathodically.

UV-Vis spectroscopy and TD-DFT calculations

In Fig. 4, the electronic absorption spectra of complexes **1**, **2**, $3{\cdot}PF_6$ and $4{\cdot}PF_6$ in CH_3CN at room temperature are presented. Below 280 nm, the spectra are dominated by π(py) → π*(py) and π(pz) → π*(pz) intraligand (IL) transitions. The absorption bands above 280 nm are mainly assigned to dπ(Re) → π*(py) and dπ(Re) → π*(pz) metal-to-ligand charge transfer transitions (MLCT). These assignments are supported by time-dependent DFT (TD-DFT) calculations of the optimized singlet geometry of the complexes (SI Fig. S30–S33 and Tables S3–S10, pages S30–S34). A common feature of the broad lowest-energy MLCT absorption is a low-intensity band, which our calculations assign to an additional MLCT transition. In complex **1**, the intense band at 308 nm is assigned to a d_{yz}(ReCl) → π*(py) (HOMO−1 → LUMO) metal–ligand-to-ligand charge-transfer transition ($MLLCT_1$). In complex **2**, the $MLLCT_1$ is observed at 348 nm, is assigned to a d_{yz}(ReCl) → π*(py) (HOMO−1 → LUMO) transition, and is red-shifted relative to complex **1**. This shift is explained by the lower energy of the LUMO in the pz-containing complex *vs.* the LUMO of the py analogue. For complex $3{\cdot}PF_6$, the $MLLCT_1$ is observed at 293 nm and is assigned to a $d_{yz}(Re^{+}NHC)$ → π*(py) (HOMO−1 → LUMO) transition. In complex $4{\cdot}PF_6$, the MLLCT1 is observed at 320 nm, and is mainly assigned to a $d_{yz}(Re^{+}NHC)$ → π*(pz) (HOMO−1 → LUMO) transition.

For all four complexes, the lowest MLCT transition ($MLLCT_2$) is described as $d_{xz}(Re^{+}NHC)$ → π*(py or pz) (HOMO → LUMO). The low molar absorptivity of the $MLLCT_2$ compared with $MLLCT_1$ can be rationalized by the orthogonality between the donor and acceptor orbitals involved in this transition. A linear correlation is observed between the energy of the $MLLCT_1$ band and the redox potential difference between the $Re^{2+/+}$ and $L^{0/-1}$ redox couples (ΔE_{ML}).[69,70] Calculated UV-Vis spectra, together with the electron density difference

maps (EDDMs) for selected transitions, can be found in the SI (Tables S3–S10, pages S30–S34).

UV-Vis spectroelectrochemistry and TD-DFT calculations

UV-Vis spectroelectrochemistry (UV-Vis-SPEC) was employed to investigate the absorption changes following one-electron oxidation and one-electron reduction of **3·PF$_6$** and **4·PF$_6$** in MeCN (0.1 M Bu_4NPF_6 0.1 M). (TD)DFT calculations were performed to support the assignments of the transitions. For complex **3**, upon one-electron oxidation a marked decrease in the intensity of the MLCT bands at 293 nm and 252 nm, along appearance of a shoulder at 267, was observed (Fig. 5). (TD)DFT assign this shoulder to MLCT transitions described as d_{yz}(Re) → π*(py)/d_{yz}(Re^+NHC) → π*(py) (Fig. S36 and Tables S11, 12, pages S37–S38). These features are consistent with the change from a d^6 to a d^5 electronic configuration of the Re(I) center. In addition, a new low-intensity band emerges at 682 nm, and according to our calculations, this transition is assigned as an NHC → d_{xz}(Re) LMCT from HOMO−4(β) to LUMO(β) (Fig. 5). The spectral changes observed upon oxidative UV-Vis-SPEC resemble those previously reported for mesoionic carbene (MIC) complexes.[71]

In complex **4·PF$_6$**, one-electron oxidation leads to similar changes in the absorption spectra (Fig. S35, page S36), including a decrease of the MLCT bands at 320 and 254 nm and the emergence of a shoulder at 427 nm. From TD-DFT calculations, this new band is predominantly assigned to contributions from NHC → π*(pz) (IL)/d_{yz}(Re) → π*(pz) (MLCT) transitions. On the other hand, in complex **4·PF$_6$**, the LMCT band (Fig. S35, page S36) is centered at 689 nm and, according to our calculations (Fig. S38 and Tables S15, 16, pages S39–40), is described as NHC → d_{xz}(Re) (HOMO−4(β) → LUMO(β)).

Spectral changes following one-electron reduction of complex **3·PF$_6$** indicate that the MLCT absorptions at 293 and 252 nm decrease in intensity, while a new broad absorption between 300 and 400 nm develops (Fig. S37, page S38). In addition, a new band appears at 443 nm. As supported by TD-DFT calculations, the broad band is mainly assigned to π*(py) → d_{yz}(Re) (LMCT) transition, whereas the band centered at 443 nm arises from π*(py) → CO (IL)/π*(py) → NHC (IL) transitions (Fig. S37 and Tables S13, S14). The changes observed after one-electron reduction of complex **4·PF$_6$** resemble those recorded for complex **3·PF$_6$**. Thus, a general increase in the absorbance between 270 and 440 nm is accompanied by the development of a new band at 484 nm (Fig. S39, page S41). According to TD-DFT calculations, these transitions are attributed to d_{yz}(Re) → CO (MLCT)/π*(pz) → NHC (IL) and π*(pz) → NHC (IL)/π*(pz) → CO (IL), respectively.

Interaction with Lewis acids

To explore how external stimuli modulate the redox properties of the cationic complexes **3·PF$_6$** and **4·PF$_6$**, we conducted cyclic voltammetry studies in the presence of Lewis acids such as $LiPF_6$ and $B(C_6F_5)_3$ in CH_3CN (0.1 M Bu_4NPF_6). The cyclic voltammetry experiments were conducted under an Ar atmosphere using the same experimental setup (WE, CE, RE) as described in the Electrochemistry section. In Fig. 6, the effect of adding $LiPF_6$ in the $Re^{2+/+}$ and $L^{0/-1}$ reduction of complexes **3·PF$_6$** and **4·PF$_6$** is shown. In complex **3·PF$_6$**, the absence of an additional nitrogen atom bearing a lone pair available for coordination serves as a control experiment to interpret the shifts in the redox couples observed upon the addition of Lewis acids in complex **4·PF$_6$**. As shown in Fig. 6, the $Re^{2+/+}$ couple in both complexes remains unchanged upon the addition of $LiPF_6$. Analysis of the voltammograms at reductive potentials shows a more pronounced effect of the addition of $LiPF_6$ on the $L^{0/-1}$ (pz) couple. This can be rationalized by assuming that Li^+ ions interact with the free nitrogen atom of the pz moiety, rendering it more electron-accepting and thereby shifting the reduction potential by ≈200 mV to more

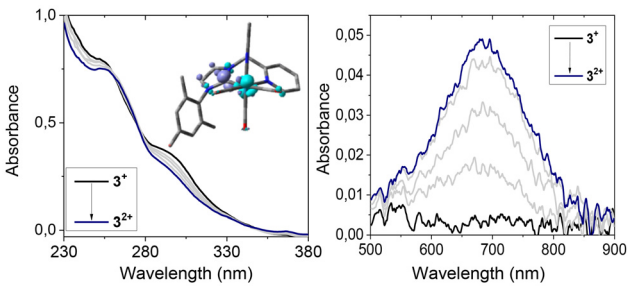

Fig. 5 UV-Vis spectroelectrochemistry for **3·PF$_6$** in CH_3CN (0.1 M Bu_4NPF_6) at room temperature. Conditions: WE (platinum), CE (platinum), and RE (Ag/AgCl 3M KCl). (*E* = 1.6 V *vs.* Ag/AgCl). EDDM of the LMCT band (#Trans 5), in which turquoise and violet colors indicate regions of increased and decreased electron density, respectively.

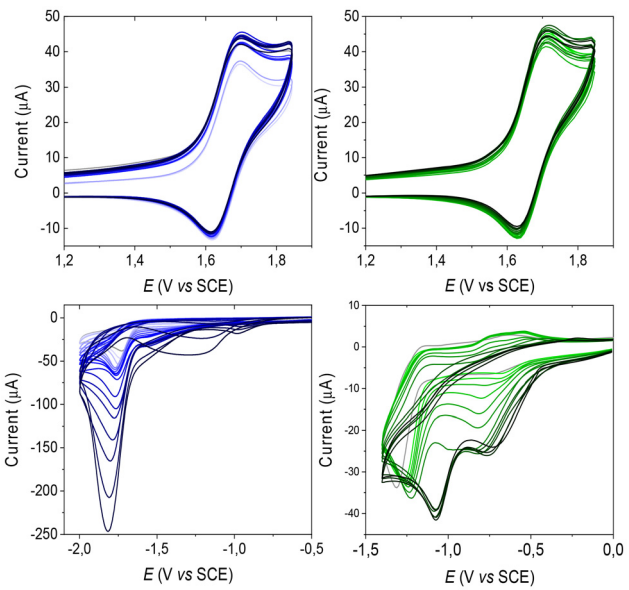

Fig. 6 Oxidative and reductive cyclic voltammetry of **3·PF$_6$** (top left and bottom left) and **4·PF$_6$** (top right and bottom right) upon successive additions of $LiPF_6$ (from light color, 1 equiv. to dark color, 22 equiv.) in CH_3CN (0.1 M Bu_4NPF_6) at 298 K. *v* = 100 mV s^{-1}. [complex] = 1.4 mM.

positive values. The electrochemical studies using $B(C_6F_5)_3$ as a strong Lewis acid yield similar results, *i.e.*, no shift in the $Re^{2+/+}$ couple and a comparable shift of the $L^{0/-1}$ (200 mV) couple in complex **4·PF$_6$** (Fig. S41). In contrast, no changes are observed in the redox potential of the $Re^{2+/+}$ and $L^{0/-1}$ (py) couples in complex **3·PF$_6$** (Fig. 6 and S40). These results are consistent with the absence of a free coordinating nitrogen atom in complex **3·PF$_6$**. The influence of $B(C_6F_5)_3$ to complex **4·PF$_6$** was also monitored by ^{1}H-NMR (Fig. S44, page S45). Thus, successive additions of the strong Lewis acid in CD_3CN solutions, deshields the protons at the pz ring and the methylene bridge, as it is observed when a strong Brønsted acid is added (*vide infra*).

Interaction with Brønsted acids

Having established the effect of Lewis acids on the redox behavior of complex **3·PF$_6$** and **4·PF$_6$**, we tested how Brønsted acids modulate their electronic properties. In contrast to Lewis acids, protonation at the N of the pz modifies the electronic structure by introducing a formal positive charge. This is expected to produce a stronger perturbation in both the metal and ligand-centered reduction processes and in the associated spectroscopic features. Protonation studies were carried out in CH_3CN (electrochemistry, IR, and UV-Vis spectroscopy) or CD_3CN (^{1}H-NMR) solutions of complex **4·PF$_6$** in the presence of trifluoromethanesulfonic acid (TfOH). Fig. 7 shows the cyclic voltammograms of complex **4·PF$_6$** with increasing equivalents of TfOH, ranging from 0 to 5.25 equiv. Upon addition of TfOH, the $Re^{2+/+}$ redox couple shifts anodically by 25 mV, indicating a small but detectable effect of protonation on the stabilization of the t_{2g} orbitals, as shown in Fig. 8. On the other hand, the ligand-centered reduction $L^{0/-1}$ (pz) shows a significant anodic shift of ≈1 V. Moreover, protonation increases the reversibility of the $L^{0/-1}$ process, thereby stabilizing the pz-reduced-complex (Fig. S43).[72] The larger shift in the $L^{0/-1}$ redox couple evidences a pronounced stabilization of the π* pz orbitals, thus decreasing the energy of the LUMO as the protonated pz becomes more electron-accepting.

This observation is supported by DFT calculations of the molecular orbitals of **4·PF$_6$-H$^+$**. Calculations also show that the LUMO+2 of complex **4·PF$_6$** becomes the LUMO+1 upon protonation, resulting in the overall stabilization of LUMO and LUMO+1 (Fig. 8). The influence of protonation on the metal-centered oxidation and ligand-centered reduction in pz-containing complexes has been described for Ru polypyridyl complexes.[44] In our model complex, the magnitude of the shift for the $L^{0/-1}$ is comparable to that reported for the Ru complexes (≈1 V). In contrast, the effect in the $Re^{2+/+}$ redox couple is approximately five times smaller than that reported for the Ru^{2+} complex. This weak response can be attributed to a lower degree of mixing between the pz and pz-H$^+$ orbitals and the $Re^{2+/+}$ orbitals compared to the Ru^{2+} complexes.

In addition to electrochemical and DFT studies, the influence of protonation was also monitored by ^{1}H-NMR (Fig. S46, page S46). Successive additions of TfOH produce a clear deshielding of the protons at the pz ring and the methylene bridge, with smaller effects observed for the carbene, acetonitrile, and mesityl protons (Fig. S47 and S48).

Finally, the impact of protonation was further studied by IR and UV-Vis spectroscopy (see Fig. 9). Upon addition of TfOH, the CO stretching frequencies move to higher wavenumbers, with corresponding shifts of $\Delta A'(1) = 5$ cm^{-1}, $\Delta A'' = 11$ cm^{-1},

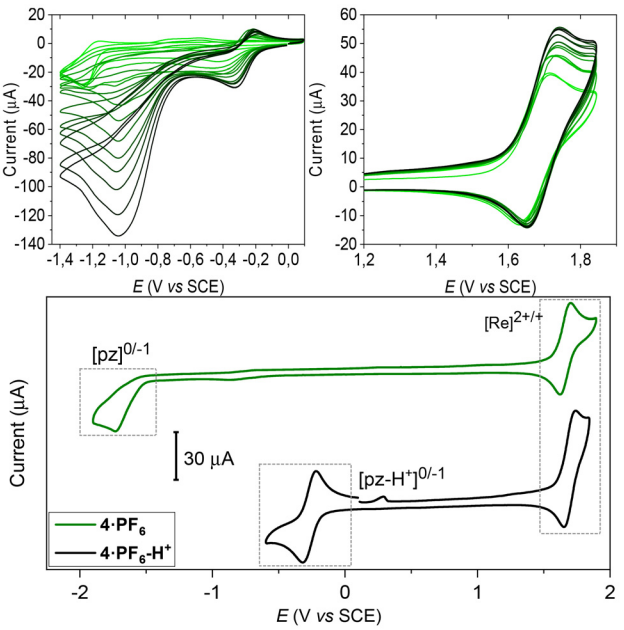

Fig. 7 Reductive (top left) and oxidative (top right) cyclic voltammetry of **4·PF$_6$** upon successive additions of TfOH (1 to 5.25 equiv.) in CH_3CN 0.1 M Bu_4NPF_6 at 298 K. v = 100 mV s^{-1}. [complex] = 1.4 mM. Cyclic voltammetry comparison of complex **4·PF$_6$** in the absence (black line) and presence (green line) of 5.25 equiv. of TfOH in CH_3CN (0.1 M Bu_4NPF_6) at 298 K. v = 100 mV s^{-1}. [complex] = 1.4 mM.

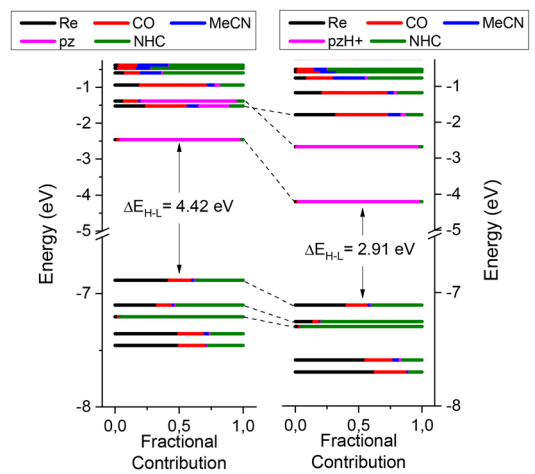

Fig. 8 DFT-calculated molecular orbital diagram for complex **4·PF$_6$** and **4·PF$_6$-H$^+$** in acetonitrile. The horizontal bars represent the contribution of each fragment to the molecular orbital composition. Fragment contributions are highlighted in black (Re), red (CO), magenta (pz), green (NHC) and blue (MeCN).

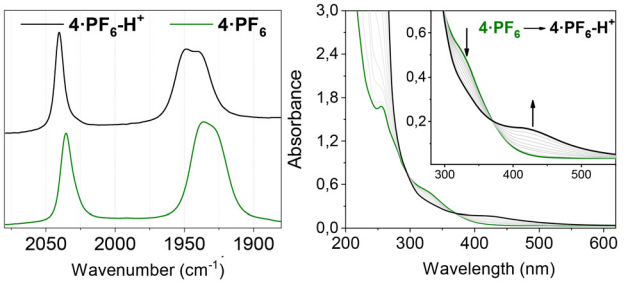

Fig. 9 Comparative IR spectra of complex **4·PF$_6$** in the absence (black line) and presence (green line) of 24 equiv. of TfOH in CH_3CN (left). UV-Vis spectral changes upon successive additions of TfOH (1 to 24 equiv.) in CH_3CN (right).

and $\Delta A'(2) = 12\ cm^{-1}$. These blue shifts are consistent with the increased electron-accepting character of the pzH$^+$ *vs.* pz ligand, thus reducing the Re → CO π-backbonding. As evidenced by the Δ values for each vibrational mode, the largest shifts correspond to the ΔA″ and ΔA′(2) modes. These are associated with the carbonyl groups *trans* to the carbene and the pz ring and, consequently, are more influenced by the protonation of the latter.

Increasing the electron-accepting character of the pz ring in **4·PF$_6$-H$^+$** induces a red shift of the dπ(Re) → π*(pz) MLLCT transitions. As shown in Fig. 9-right, protonation of the pz leads to a decrease in the intensity of the band at 320 nm while a new band develops at 415 nm. These changes are accompanied by well-defined isosbestic points at 300 and 369 nm, indicating that two species are in equilibrium. The observed behavior is consistent with the stabilization of the π* (pz) orbitals, as evidenced in the cyclic voltammograms of **4·PF$_6$-H$^+$** and supported by DFT calculations. Moreover, the linear correlation between the energy of the lowest MLLCT transition and ΔE_{ML}, in agreement with the Lever relationship, confirms the nature of the transition (Fig. S49).

Conclusions

We have synthesized and characterized four Re(I)-complexes bearing NHC-based ligands. The synthesized complexes have been fully characterized by spectroscopic, electrochemical, and diffraction techniques, and the results have been rationalized using DFT and TD-DFT calculations. Incorporation of a pz ring in the ligand structure renders the $L^{0/-1}$ redox couple in complex **4·PF$_6$** responsive to external stimuli such as Brønsted or Lewis acid. The results shown indicate that the addition of a proton source drastically affects the electronic structure of complex **4·PF$_6$** relative to **3·PF$_6$**, as evidenced in their UV-Vis, NMR, and IR spectra, as well as electrochemical response (ligand-centered reduction $L^{0/-1}$ shifted by ≈0.90 V). The results described herein advance the understanding of pz-based complexes. Our next step is to use the developed systems to create heterobimetallic assemblies that enable the exploration of distinct metal–ligand and metal-to-metal cooperative effects.

Author contributions

F. J. R. synthesized and characterized the ligands and all the neutral complexes; P. O. A. synthesized the cationic complexes and performed all spectroscopic and electrochemical measurements, as well as DFT and TD-DFT calculations; F. J. F. C. performed and solved the XRD data; A. R co-supervised the synthetic procedures of ligand and complexes; O. R. W. conceived and supervised the study, and wrote the manuscript with input from P. O. A. and A. R.

Conflicts of interest

There are no conflicts to declare.

Data availability

The data supporting this article have been included as part of the supplementary information (SI). Supplementary information: General information and materials; synthesis of azolium salts, neutral Re-complexes, and cationic recomplexes; NMR, IR and HRMS spectra; electrochemistry; DFT calculations of the singlet and doublet ground state; (TD)TDF of the singlet ground state; UV-Vis spectroelectrochemistry; (TD)TDF of the one-electron oxidized and one-electron reduced species of 3 and 4 in their singlet ground stae; acid effects: electrochemistry and ^{1}H NMR spectra. See DOI: https://doi.org/10.1039/d6dt00158k.

CCDC 2516342 (**2**), 2516343 (**3·PF6**) and 2516344 (**4·BF4**) contain the supplementary crystallographic data for this paper.[73a–c]

The Cartesian coordinates of optimized compounds can be found in a sepatate file in the supplementary files.

Acknowledgements

The authors greatly acknowledge the financial support through the grants CNS2022-135765, RED2018-102387-T, RYC2020-028851-I funded by MCIN/AEI/10.13039/501100011033; the Junta de Andalucía through the grant PROYEXCEL_00746; and the financial support received from the Universidad de Sevilla through the program TALENTO. The use of computational facilities of the Super-computing Centre of Galicia (CESGA) is gratefully acknowledged. We thank Dr Noa Burshtein for scientific editing of the manuscript.

References

1 R. H. Crabtree, Multifunctional ligands in transition metal catalysis, *New J. Chem.*, 2011, **35**, 18–23.
2 J. R. Khusnutdinova and D. Milstein, Metal–ligand cooperation, *Angew. Chem., Int. Ed.*, 2015, **54**, 12236–12273.

3 M. Loipersberger, D. G. A. Cabral, D. B. K. Chu and M. Head-Gordon, Mechanistic insights into Co and Fe quaterpyridine-based CO2 reduction catalysts: metal–ligand orbital interaction as the key driving force for distinct pathways, *J. Am. Chem. Soc.*, 2021, **143**, 744–763.
4 M. R. Elsby and R. T. Baker, Strategies and mechanisms of metal–ligand cooperativity in first-row transition metal complex catalysts, *Chem. Soc. Rev.*, 2020, **49**, 8933–8987.
5 B. S. Cooperman, Coordination chemistry and biology, in *Encyclopedia of Biological Chemistry*, ed. W. J. Lennarz and M. D. Lane, Academic Press, Waltham, 2nd edn, 2013, pp. 71–74.
6 N. C. Gianneschi, M. S. Masar and C. A. Mirkin, Development of a coordination chemistry-based approach for functional supramolecular structures, *Acc. Chem. Res.*, 2005, **38**, 825–837.
7 A. M. Lifschitz, M. S. Rosen, C. M. McGuirk and C. A. Mirkin, Allosteric supramolecular coordination constructs, *J. Am. Chem. Soc.*, 2015, **137**, 7252–7261.
8 M. C. T. Fyfe and J. F. Stoddart, Synthetic supramolecular chemistry, *Acc. Chem. Res.*, 1997, **30**, 393–401.
9 B. Y. Lee, G. C. Bazan, J. Vela, Z. J. A. Komon and X. Bu, α-Iminocarboxamidato–Nickel(II) ethylene polymerization catalysts, *J. Am. Chem. Soc.*, 2001, **123**, 5352–5353.
10 J. D. Azoulay, Z. A. Koretz, G. Wu and G. C. Bazan, Well-defined cationic methallyl α-keto-β-diimine complexes of nickel, *Angew. Chem., Int. Ed.*, 2010, **49**, 7890–7894.
11 N. G. Léonard, R. Dhaoui, T. Chantarojsiri and J. Y. Yang, Electric fields in catalysis: from enzymes to molecular catalysts, *ACS Catal.*, 2021, **11**, 10923–10932.
12 S. Acosta-Calle and A. J. M. Miller, Tunable and switchable catalysis enabled by cation-controlled gating with crown ether ligands, *Acc. Chem. Res.*, 2023, **56**, 971–981.
13 K. Guo, S. Yang, Y. Wang, Y. Zhong, B. Chen, J. Yi, Y. Liu, M. Pan, H. Yuan, L. Jiang and Z. Han, Self-sensitized cobalt molecular photocatalysts: the effects of alkali cations on tuning the activity of H2 production, *ACS Catal.*, 2025, **15**, 18769–18781.
14 A. D. Dilinaer, G. J. Jobin and M. W. Drover, A catalytic collaboration: pairing transition metals and Lewis acids for applications in organic synthesis, *Dalton Trans.*, 2024, **53**, 13298–13307.
15 S. Acosta-Calle, E. Z. Huebsch, S. S. Kolmar, M. T. Whited, C.-H. Chen and A. J. M. Miller, Regulating access to active sites via hydrogen bonding and cation–dipole interactions: a dual cofactor approach to switchable catalysis, *J. Am. Chem. Soc.*, 2024, **146**, 11095–11104.
16 E. Huebsch, S. Acosta-Calle, G. A. Richter, J. E. Halenda, Z. E. Stuart, C.-H. Chen and A. Miller, A flexidentate bipyridine-aza-crown ether ligand enables cation-tunable nickel redox properties, *Inorg. Chem.*, 2026, **65**, 1930–1942.
17 M. Delgado, J. M. Ziegler, T. Seda, L. N. Zakharov and J. D. Gilbertson, Pyridinediimine iron complexes with pendant redox-inactive metals located in the secondary coordination sphere, *Inorg. Chem.*, 2016, **55**, 555–557.
18 J. P. Karnes, N. M. Lind, A. G. Oliver, C. S. Day, V. W. Day and J. D. Blakemore, Tunability in heterobimetallic complexes featuring an acyclic "Tiara" polyether motif, *Inorg. Chem.*, 2025, **64**, 571–593.
19 P. Teptarakulkarn, W. Lorpaiboon, T. Anusanti, N. Laowiwatkasem, K. Chainok, P. Sangtrirutnugul, P. Surawatanawong and T. Chantarojsiri, Incorporation of cation affects the redox reactivity of Fe–NNN complexes on C–H oxidation, *Inorg. Chem.*, 2022, **61**, 11066–11074.
20 A. H. Reath, J. W. Ziller, C. Tsay, A. J. Ryan and J. Y. Yang, Redox potential and electronic structure effects of proximal nonredox active cations in cobalt Schiff base complexes, *Inorg. Chem.*, 2017, **56**, 3713–3718.
21 K. H. S. Eisenhardt, F. Fiorentini, F. Butler, R. Thorogood and C. K. Williams, General, quantified structure-performance correlations for synergistic heteronuclear electro-, polymerization, and asymmetric catalysts, *ACS Catal.*, 2025, **15**, 12959–12983R.
22 E. R. Mikeska and J. D. Blakemore, Differentiating ligand tailoring and cation incorporation as strategies for tuning heterobimetallic cerium complexes, *Chem. – Eur. J.*, 2025, **31**, e202500474.
23 D. E. Herbert, D. Lionetti, J. Rittle and T. Agapie, Heterometallic triiron-oxo/hydroxo clusters: effect of redox-inactive metals, *J. Am. Chem. Soc.*, 2013, **135**, 19075–19078.
24 H. M. Nguyen, H. W. T. Morgan, T. Chantarojsiri, T. A. Kerr, J. Y. Yang, A. N. Alexandrova and N. G. Léonard, Charge and solvent effects on the redox behavior of vanadyl salen-crown complexes, *J. Phys. Chem. A*, 2023, **127**, 5324–5334.
25 T. Chantarojsiri, J. W. Ziller and J. Y. Yang, Incorporation of redox-inactive cations promotes iron catalyzed aerobic C–H oxidation at mild potentials, *Chem. Sci.*, 2018, **9**, 2567–2574.
26 E. Y. Tsui, R. Tran, J. Yano and T. Agapie, Redox-inactive metals modulate the reduction potential in heterometallic manganese-oxido clusters, *Nat. Chem.*, 2013, **5**, 293–299.
27 D. Lionetti, S. Suseno, A. A. Shiau, G. de Ruiter and T. Agapie, Redox processes involving oxygen: the surprising influence of redox-inactive Lewis acids, *JACS Au*, 2024, **4**, 344–368.
28 J. M. Barlow, J. W. Ziller and J. Y. Yang, Inhibiting the hydrogen evolution reaction (HER) with proximal cations: a strategy for promoting selective electrocatalytic reduction, *ACS Catal.*, 2021, **11**, 8155–8164.
29 N. A. Swisher and R. H. Grubbs, Synthesis and characterization of 3,5-Bis(di-tert-butylphosphinito)pyridine pincer complexes, *Organometallics*, 2020, **39**, 2479–2485.
30 T. M. Bhatti, A. Kumar, A. Parihar, H. K. Moncy, T. J. Emge, K. M. Waldie, F. Hasanayn and A. S. Goldman, Metal–ligand proton tautomerism, electron transfer, and C(sp^3)–H activation by a 4-pyridinyl-pincer iridium hydride complex, *J. Am. Chem. Soc.*, 2023, **145**, 18296–18306.
31 A. L. Liberman-Martin, M. S. Ziegler, A. G. DiPasquale, R. G. Bergman and T. D. Tilley, Functionalization of an iridium–diamidocarbene complex by ligand-based reac-

tions with titanocene and zirconocene sources, *Polyhedron*, 2016, **116**, 111–115.

32 A. L. Liberman-Martin, R. G. Bergman and T. D. Tilley, A remote Lewis acid trigger dramatically accelerates biaryl reductive elimination from a platinum complex, *J. Am. Chem. Soc.*, 2013, **135**, 9612–9615.

33 A. L. Liberman-Martin, D. S. Levine, W. Liu, R. G. Bergman and T. D. Tilley, Biaryl reductive elimination is dramatically accelerated by remote Lewis acid binding to a 2,2′-bipyrimidyl-platinum complex: evidence for a bidentate ligand dissociation mechanism, *Organometallics*, 2016, **35**, 1064–1069.

34 J. P. Shanahan, C. M. Moore, J. W. Kampf and N. K. Szymczak, Modulation of H^+/H^- exchange in iridium-hydride 2-hydroxypyridine complexes by remote Lewis acids, *Chem. Commun.*, 2021, **57**, 11705–11708.

35 K. T. Horak, D. G. VanderVelde and T. Agapie, Tuning of metal complex electronics and reactivity by remote Lewis acid binding to π-coordinated pyridine diphosphine ligands, *Organometallics*, 2015, **34**, 4753–4765.

36 A. Srinivasan, J. Campos, N. Giraud, M. Robert and O. Rivada-Wheelaghan, MnI complex redox potential tunability by remote Lewis acid interaction, *Dalton Trans.*, 2020, **49**, 16623–16626.

37 J. W. Jurss, R. S. Khnayzer, J. A. Panetier, K. A. El Roz, E. M. Nichols, M. Head-Gordon, J. R. Long, F. N. Castellano and C. J. Chang, Bioinspired design of redox-active ligands for multielectron catalysis: effects of positioning pyrazine reservoirs on cobalt for electro- and photocatalytic generation of hydrogen from water, *Chem. Sci.*, 2015, **6**, 4954–4972.

38 R. A. Periana, D. J. Taube, S. Gamble, H. Taube, T. Satoh and H. Fujii, Platinum catalysts for the high-yield oxidation of methane to a methanol derivative, *Science*, 1998, **280**, 560–564.

39 D. Lou, N. J. Yutronkie, I. Oyarzabal, L.-F. Wang, A. Adak, V. L. Nadurata, R. Diego, E. A. Suturina, A. Mailman, P. Dechambenoit, M. Rouzières, F. Wilhelm, A. Rogalev, S. Bonhommeau, C. Mathonière and R. Clérac, Self-assembled tetranuclear square complex of chromium(III) bridged by radical pyrazine: a molecular model for metal–organic magnets, *J. Am. Chem. Soc.*, 2024, **146**, 19649–19653.

40 O. Rivada-Wheelaghan, A. Dauth, G. Leitus, Y. Diskin-Posner and D. Milstein, Synthesis and reactivity of iron complexes with a new pyrazine-based pincer ligand, and application in catalytic low-pressure hydrogenation of carbon dioxide, *Inorg. Chem.*, 2015, **54**, 4526–4538.

41 P. H. Dinolfo, M. E. Williams, C. L. Stern and J. T. Hupp, Rhenium-based molecular rectangles as frameworks for ligand-centered mixed valency and optical electron transfer, *J. Am. Chem. Soc.*, 2004, **126**, 12989–13001.

42 K. D. Demadis, C. M. Hartshorn and T. J. Meyer, The localized-to-delocalized transition in mixed-valence chemistry, *Chem. Rev.*, 2001, **101**, 2655–2686.

43 L. S. Xie, G. Skorupskii and M. Dincă, Electrically conductive metal-organic frameworks, *Chem. Rev.*, 2020, **120**, 8536–8580.

44 I. Ramírez-Wierzbicki, G. E. Pieslinger, B. M. Aramburu-Trošelj, P. O. Abate and A. Cadranel, Ru monoimines with extended excited-state lifetimes and geometrical modulation of photoinduced mixed-valence interactions, *Inorg. Chem.*, 2023, **62**, 3808–3816.

45 J. S. Doll, F. J. Becker and D.-A. Roşca, Diazines and triazines as building blocks in ligands for metal-mediated catalytic transformations, *ACS Org. Inorg. Au*, 2024, **4**, 41–58.

46 I. Haiduc, Inverse coordination. Organic nitrogen heterocycles as coordination centers. A survey of molecular topologies and systematization. Part 2. Six-membered rings, *J. Coord. Chem.*, 2019, **72**, 2805–2903.

47 A. S. Hazari, A. Indra and G. K. Lahiri, Mixed valency in ligand-bridged diruthenium frameworks: divergences and perspectives, *RSC Adv.*, 2018, **8**, 28895–28908.

48 N. I. Regenauer, S. Jänner, H. Wadepohl and D.-A. Roşca, A redox-active heterobimetallic N-heterocyclic carbene based on a bis(imino)pyrazine ligand scaffold, *Angew. Chem., Int. Ed.*, 2020, **59**, 19320–19328.

49 D. Sanchez Arana, J. R. Billups, B. Donnadieu and S. E. Creutz, Synthesis and electronic structure of a series of first-row transition-metal pyrazine(diimine) complexes in two oxidation states, *J. Coord. Chem.*, 2022, **75**, 1815–1840.

50 W. Aoki, N. Wattanavinin, S. Kusumoto and K. Nozaki, Development of highly active Ir–PNP catalysts for hydrogenation of carbon dioxide with organic bases, *Bull. Chem. Soc. Jpn.*, 2016, **89**, 113–124.

51 M. D. Walter, P. S. White, C. K. Schauer and M. Brookhart, The quest for stable σ-methane complexes: computational and experimental studies, *New J. Chem.*, 2011, **35**, 2884–2893.

52 M. Darari, E. Domenichini, A. Francés-Monerris, C. Cebrián, K. Magra, M. Beley, M. Pastore, A. Monari, X. Assfeld, S. Haacke and P. C. Gros, Iron(II) complexes with diazinyl-NHC ligands: impact of π-deficiency of the azine core on photophysical properties, *Dalton Trans.*, 2019, **48**, 10915–10926.

53 U. Eiermann, C. Krieger, F. A. Neugebauer and H. A. Staab, 2.2- and 2.2Pyrazinophanes: synthesis and molecular structure, *Chem. Ber.*, 1990, **123**, 523–533.

54 X.-W. Li, H.-Y. Li, G.-F. Wang, F. Chen, Y.-Z. Li, X.-T. Chen, Y.-X. Zheng and Z.-L. Xue, Blue-green luminescent rhenium(I) tricarbonyl complexes with pyridine-functionalized N-heterocyclic carbene ligands, *Organometallics*, 2012, **31**, 3829–3835.

55 L. A. Worl, R. Duesing, P. Chen, L. D. Ciana and T. J. Meyer, Photophysical properties of polypyridyl carbonyl complexes of rhenium(I), *J. Chem. Soc., Dalton Trans.*, 1991, 849–858.

56 J. A. Baiano, D. L. Carlson, G. M. Wolosh, D. E. DeJesus, C. F. Knowles, E. G. Szabo and W. R. Murphy Jr., Bimetallic complexes of rhenium(I). Preparation of Re(BL)(CO)3Cl and

[Re(CO)3Cl]2(BL) (BL = 2,3-bis(2-pyridyl)pyrazine, 2,3-bis(2-pyridyl)quinoxaline, and 2,3-bis(2-pyridyl)benzo[g]quinoxaline), *Inorg. Chem.*, 1990, **29**, 2327–2332.

57 G. J. Stor, F. Hartl, J. W. M. van Outersterp and D. J. Stufkens, Spectroelectrochemical (IR, UV/Vis) determination of the reduction pathways for a series of [Re(CO)3(α-diimine)L′]0/+ (L′ = halide, OTf–, THF, MeCN, n-PrCN, PPh3, P(OMe)3) complexes, *Organometallics*, 1995, **14**, 1115–1131.

58 A. V. Müller, W. M. Wierzba, L. G. A. do Nascimento, J. J. Concepcion, S. Nikolaou, D. E. Polyansky and A. S. Polo, Electrochemical and spectroscopic investigation of molecular catalysts for solar fuel production: activity, selectivity, and mechanisms, *Artif. Photosynth.*, 2025, **1**, 214–225.

59 J. P. Bullock, E. Carter, R. Johnson, A. T. Kennedy, S. E. Key, B. J. Kraft, D. Saxon and P. Underwood, Reactivity of electrochemically generated rhenium(II) tricarbonyl α-diimine complexes: a reinvestigation of the oxidation of luminescent Re(CO)3(α-diimine)Cl and related compounds, *Inorg. Chem.*, 2008, **47**, 7880–7887.

60 A. J. Bard and L. R. Faulkner, *Electrochemical Methods: Fundamentals and Applications*, Willey, 2nd edn, 2011.

61 J. P. Perdew, K. Burke and M. Ernzerhof, Generalized Gradient Approximation Made Simple, *Phys. Rev. Lett.*, 1996, **77**, 3865–3868.

62 A. D. Becke, Density functional calculations of molecular bond energies, *J. Chem. Phys.*, 1986, **84**, 4524–4529.

63 A. D. Becke, Density–functional thermochemistry. I. The effect of the exchange–only gradient correction, *J. Chem. Phys.*, 1992, **96**, 2155–2160.

64 C. Lee, W. Yang and R. G. Parr, Development of the Colle-Salvetti correlation-energy formula into a functional of the electron density, *Phys. Rev. B: Condens. Matter Mater. Phys.*, 1988, **37**, 785–789.

65 S. Grimme, S. Ehrlich and L. Goerigk, Effect of the damping function in dispersion corrected density functional theory, *J. Comput. Chem.*, 2011, **32**, 1456–1465.

66 S. Grimme, J. Antony, S. Ehrlich and H. Krieg, A consistent and accurate ab initio parametrization of density functional dispersion correction (DFT-D) for the 94 elements H-Pu, *J. Chem. Phys.*, 2010, **132**, 154104.

67 V. Barone and M. Cossi, Quantum Calculation of Molecular Energies and Energy Gradients in Solution by a Conductor Solvent Model, *J. Phys. Chem. A*, 1998, **102**, 1995–2001.

68 M. Cossi, N. Rega, G. Scalmani and V. Barone, Energies, structures, and electronic properties of molecules in solution with the C-PCM solvation model, *J. Comput. Chem.*, 2003, **24**, 669–681.

69 E. S. Dodsworth and A. B. P. Lever, Vibrational and electronic spectra of charge-transfer excited states of polypyridine complexes, *Chem. Phys. Lett.*, 1984, **112**, 567–570.

70 E. S. Dodsworth and A. B. P. Lever, Relationships between electronic spectroscopy and electrochemistry: a probe of reorganisation energies, *Chem. Phys. Lett.*, 1985, **119**, 61–66.

71 A. Wilting, T. Stolper, R. A. Mata and I. Siewert, Dinuclear rhenium complex with a proton responsive ligand as a redox catalyst for the electrochemical CO_2 reduction, *Inorg. Chem.*, 2017, **56**, 4176–4185.

72 M. Zafar, V. Subramaniyan, F. Tibika and Y. Tulchinsky, Cationic ligands – from monodentate to pincer systems, *Chem. Commun.*, 2024, **60**, 9871–9906.

73 (*a*) CCDC 2516342: Experimental Crystal Structure Determination, 2026, DOI: 10.5517/ccdc.csd.cc2qggb0; (*b*) CCDC 2516343: Experimental Crystal Structure Determination, 2026, DOI: 10.5517/ccdc.csd.cc2qggc1; (*c*) CCDC 2516344: Experimental Crystal Structure Determination, 2026, DOI: 10.5517/ccdc.csd.cc2qggd2.